Melting and phase relations of Fe-Ni-Si determined by a multi-technique approach

Vasilije V. Dobrosavljevic [a,*], Dongzhou Zhang [b], Wolfgang Sturhahn [a], Jiyong Zhao [c], Thomas S. Toellner [c], Stella Chariton [d], Vitali B. Prakapenka [d], Olivia S. Pardo [a], Jennifer M. Jackson [a]

[a] *Seismological Laboratory, Division of Geological and Planetary Sciences, California Institute of Technology, Pasadena, CA, USA*
[b] *Hawai'i Institute of Geophysics and Planetology, University of Hawai'i at Mānoa, Honolulu, HI, USA*
[c] *Advanced Photon Source, Argonne National Laboratory, Chicago, IL, USA*
[d] *Center for Advanced Radiation Sources, The University of Chicago, Chicago, IL, USA*

ARTICLE INFO

ABSTRACT

Many studies have suggested silicon as a candidate light element for the cores of Earth and Mercury. However, the effect of silicon on the melting temperatures of core materials and thermal profiles of cores is poorly understood, due to disagreements among melt detection techniques, uncertainties in sample pressure evolution during heating, and sparsity of studies investigating the combined effects of nickel and silicon on the phase diagram of iron. In this study we develop a multi-technique approach for measuring the high-pressure melting and solid phase relations of iron alloys and apply it to $Fe_{0.8}Ni_{0.1}Si_{0.1}$ (Fe-11wt%Ni-5.3wt%Si), a composition compatible with recent estimates for the cores of Earth and Mercury. This approach combines results (20-83 GPa) from two atomic-level techniques: synchrotron Mössbauer spectroscopy (SMS) and synchrotron x-ray diffraction (XRD). Melting is independently detected by the loss of the Mössbauer signal, produced exclusively by solid-bound iron nuclei, and the onset of a liquid diffuse x-ray scattering signal. The use of a burst heating and background updating method for quantifying changes in the reference background during heating facilitates the determination of liquid diffuse signal onsets and leads to strong reproducibility and excellent agreement in melting temperatures determined separately by the two techniques. XRD measurements additionally constrain the *hcp-fcc* phase boundary and *in-situ* pressure evolution of the samples during heating. We apply our updated thermal pressure model to published SMS melting data on *fcc*-Fe and *fcc*-$Fe_{0.9}Ni_{0.1}$ to precisely evaluate the effect of silicon on melting temperatures. We find that the addition of 10 mol% Si to $Fe_{0.9}Ni_{0.1}$ reduces melting temperatures by ∼250 K at low pressures (<60 GPa) and flattens the *hcp-fcc* phase boundary. Extrapolating our results, we constrain the location of the *hcp-fcc-liquid* quasi-triple point at 147±14 GPa and 3140±90 K, which implies a melting temperature reduction of 500 K compared with $Fe_{0.9}Ni_{0.1}$. The results demonstrate the advantages of combining complementary experimental techniques in investigations of melting under extreme conditions.

© 2021 Elsevier B.V. All rights reserved.

1. Introduction

The metallic cores of terrestrial planets in our solar system are suggested to be composed of iron alloyed with nickel (∼5wt%) and candidate light elements, based on cosmochemical studies, planetary accretion models, and seismological constraints in the case of the Earth (McDonough and Sun, 1995; Sohl and Schubert, 2007; Hirose et al., 2013). Constraints on temperature profiles and thermal evolution models of terrestrial planets (e.g., Knibbe and van Westrenen, 2018) have benefited from high-pressure experimental studies on the melting curves of iron and iron alloys (e.g., Morard et al., 2011; Zhang et al., 2016; Anzellini et al., 2013; Sinmyo et al., 2019). Accurate constraints on core temperatures are essential for understanding major processes like inner core crystallization (Labrosse et al., 2001), magnetic field generation (Olson, 2013), and heat flow through the core-mantle boundary (Lay et al., 2008), as well as the compositions, phase relations, and dynamics of complex multiscale structures in Earth's lowermost mantle (e.g., Jackson and Thomas, 2021; Dobrosavljevic et al., 2019; Li, 2020; Dannberg et al., 2021). The presence of moderate amounts of light

elements such as Si, O, C, S, and H has consistently been shown to depress the melting temperatures of iron alloys, though their effects on the temperatures and shapes of melting curves remain challenging to constrain due to disagreements across the range of studies and experimental techniques (reviewed by Fischer, 2016).

Silicon has commonly been proposed as a candidate light element for several terrestrial planetary cores. Its suggested presence in Earth's core has been inferred from its abundance in the silicate mantle, its solubility in liquid iron (Ozawa et al., 2009), and discrepancies between its isotopic composition in meteorites and the bulk silicate Earth (Shahar et al., 2009; Hin et al., 2014). Concentration estimates are generally placed between 1 to 11wt%Si (e.g., Morrison et al., 2018; Javoy et al., 2010; Ricolleau et al., 2011). In the case of Mercury's core, the presence of silicon has been inferred from analyses of magnetic field and surface chemistry data collected by the recent MESSENGER mission (Knibbe and van Westrenen, 2018; Steenstra and van Westrenen, 2020), with suggested concentrations ranging from 1 to 20wt%Si dependent on the presence of carbon or sulfur (Knibbe et al., 2021).

Very few studies, however, have investigated the combined effects of silicon and nickel on the high-pressure and temperature phase boundaries of iron. For the melting of Fe-Ni-Si, experimental studies are limited to one static compression study (Morard et al., 2011) and one shock compression study (Zhang et al., 2018). The few melting studies on Fe-Si compositions without nickel show discrepant results, with some suggestion of elevated melting temperatures relative to iron, and are limited to relatively large Si concentrations (>9wt%) (Lord et al., 2010; Asanuma et al., 2010; Fischer et al., 2012, 2013). Solid-solid phase boundaries, which also affect high-pressure melting and the location of solid-solid-liquid triple points, are dependent on Si concentration (Fischer et al., 2013; Wicks et al., 2018) and the presence of nickel (Torchio et al., 2020), further complicating interpretations of melting results. The only study on solid phase boundaries of Fe-Ni-Si measured a flattening of the *hcp-fcc* boundary relative to Fe that could not be predicted from separate measurements of Fe-Ni and Fe-Si (Komabayashi et al., 2019b).

In this work we develop a multi-technique approach for measuring the high-pressure melting and solid phase relations of iron alloys. We compress samples from an identical source in laser-heated diamond anvil cells using identical preparation procedures. Melting is detected with two independent *in-situ* atomic-level techniques: synchrotron Mössbauer spectroscopy (SMS), sensitive exclusively to the dynamics of solid-bound ^{57}Fe nuclei, and synchrotron x-ray diffraction (XRD), sensitive to the loss of long-range crystalline order due to melting. SMS measurements feature a high-frequency temperature readout system (Zhang et al., 2015) that monitors rapid temporal fluctuations to improve precision on temperature measurements. XRD measurements constrain the *hcp-fcc* phase boundary and thermal pressure evolution of the samples, and are conducted using a burst heating with reference background updating method to quantify changes to the reference background during heating. We apply this multi-technique approach to studying the phase diagram of Fe$_{0.8}$Ni$_{0.1}$Si$_{0.1}$ (Fe-11wt%Ni-5.3wt%Si), a candidate composition for planetary cores that has been shown to satisfy seismic observational constraints of the density, bulk modulus, and bulk sound speed of Earth's inner core boundary (Morrison et al., 2018).

2. Methods

2.1. Sample preparation

Samples of Fe$_{0.8}$Ni$_{0.1}$Si$_{0.1}$, previously studied by Morrison et al. (2018, 2019), were cut into rectangular sections with lateral dimensions of 30 to 100 μm and thickness of ∼10 μm and loaded in

diamond anvil cells (DACs) with rhenium gaskets serving as sample chambers. Samples were sandwiched inside the sample chamber between flakes of dehydrated KCl with a minimum thickness of 10 μm that served as both thermal insulation and a pressure transmitting medium. At least one ruby sphere was loaded into the sample chamber without contact with the sample. Once loaded, each DAC was heated in a vacuum oven for 12 to 24 hours in order to minimize oxygen and moisture in the sample chamber, then subsequently sealed and compressed to its target pressure. Starting pressures were estimated from ruby fluorescence and measured by XRD (see Section 3.3). All samples for both sets of experiments were cut from the same bulk material and prepared using identical methods (see Text S1 for further details).

2.2. Phase detection techniques

2.2.1. Synchrotron Mössbauer spectroscopy

Synchrotron Mössbauer spectroscopy (SMS) is a nuclear resonant forward scattering technique that involves the excitation of the first excited state of the ^{57}Fe nucleus, characterized by a transition energy of 14.4 keV and an excitation lifetime of 141 ns (Jackson et al., 2013; Sturhahn, 2000, 2004). In the scattering process, most photons from the incident synchrotron x-ray beam are scattered by the sample's electrons in femtoseconds. Some photons, however, excite the ^{57}Fe nucleus and are re-emitted as the nucleus decays back to its ground state. A finite fraction of excitation events results in recoil-free absorption and emission of photons by the sample with no transfer of momentum between the photons and the iron nuclei, known as the Mössbauer effect. Nuclear resonant forward scattering is a coherent, elastic scattering process that is proportional to the Lamb-Mössbauer factor $f_{LM} = e^{-k^2 \langle u^2 \rangle}$, where f_{LM} is the probability of recoil-free excitation events, k is the wavenumber of the incident photon (1.161×10^8 cm^{-1}), and $\langle u^2 \rangle$ is the mean-square displacement of the nucleus. By measuring forward scattered, time-delayed photons, one can isolate the Mössbauer signal that originates exclusively from the solid-bound ^{57}Fe nuclei.

The Mössbauer signal has been demonstrated to be an effective probe for detecting melting in Fe and Fe-Ni (Jackson et al., 2013; Zhang et al., 2016). As the sample is heated to its melting temperature, a loss of signal intensity indicates a loss of coherence in the scattering process, meaning that the iron atoms are no longer bound by the solid sample within the lifetime of the nuclear excitation. As the finite displacement of the solid-bound nucleus becomes very large upon melting, the measured signal and the Lamb-Mössbauer factor begin dropping off to zero, giving a signature of melting that can be fit with an experiment-specific scattering intensity model. The SMS technique thus directly probes the dynamic behavior of the iron atoms in order to detect melting. Because the Mössbauer signal originates exclusively from solid-bound iron nuclei, no other components in the sample assemblage or experimental setup contribute to the signal, resulting in negligible background and allowing for clear demarcation of the first onset of melt.

2.2.2. X-ray diffraction

Synchrotron X-ray diffraction (XRD) is an *in-situ* technique sensitive to atomic positions, with the electronic scattering process occurring at extremely fast timescales (on the order of 10^{-19} seconds). The presence of melt in the sample is revealed by the appearance of a diffuse scattering signal, originating from atomic disorder in the liquid state. This particular signal, termed liquid diffuse scattering, is characterized by a discontinuous increase in background intensity. The appearance of a liquid diffuse scattering signal has been used in previous studies for detecting melting at high pressures in iron and iron alloys (e.g., Anzellini et al., 2013;

Morard et al., 2011; Boehler et al., 2008). XRD measurements additionally provide several other valuable pieces of information. Structural information is used to constrain the *hcp-fcc* phase boundary and monitor signals of chemical contamination. Unit-cell volumes measured at each temperature are used to calculate *in-situ* sample pressure evolution through the heating run using previously published thermal equations of state for the sample and the surrounding KCl, thus reducing a large source of uncertainty in constructing the phase boundaries at high-P, T conditions. Finally, changes in sample pressure during the XRD heating run can be fit and applied to the SMS measurements, where sample preparations are essentially identical but pre-melting information on the sample's unit-cell volume (and thus pressure) is unavailable.

2.3. Experimental procedures

2.3.1. Synchrotron Mössbauer spectroscopy

The SMS experiments are conducted at beamline 3-ID-B of the Advanced Photon Source, which features resonant scattering techniques coupled with double-sided laser heating, the high-frequency FasTeR temperature measurement system (Zhang et al., 2015), conventional CCD-based upstream and downstream spectrometers, and x-ray diffraction (XRD). These experiments are conducted in top-up mode with 24 photon bunches separated by 153 ns. X-rays are prepared with a bandwidth of 1 meV at the 14.4125 keV nuclear resonance of ^{57}Fe using a silicon high-resolution monochromator (Toellner, 2000). The signal is recorded using an avalanche photodiode detector (APD) in forward scattering geometry. Ionization chambers are placed proximal to the DAC (upstream and downstream) to record fluctuations in the incident x-ray intensity and x-ray intensity absorption through the DAC assemblage, to monitor the thickness of the sample chamber during heating.

The shape and full-width half-maximum (FWHM $\sim$16x16 μm^2) of the x-ray beam are measured by knife-edge scans using tungsten rods. Upstream and downstream cameras are optically aligned to the DAC position, while the DAC is aligned to the x-ray position using delay count intensities measured by horizontal and vertical scans of the sample chamber. Alignment of the laser hotspot (FWHM $\sim$35x35 μm^2) and the x-ray beam are visually verified immediately before and after each heating run with cameras, and small changes in hotspot position due to thermal expansion of laser optics are monitored during heating runs and fit during data analysis (Section 3.2.1). XRD images are collected immediately before and after each heating run using a movable high resolution MAR345 image plate (Marresearch GmbH). Due to the meV bandwidth and the 14.4 keV incident energy, the exposure time required for a reasonable quality diffraction image is about 20 minutes. A CeO$_2$ standard is used to calibrate the sample and image plate geometry. Samples are initially heated to $\sim$1500 K for at least 5 minutes in order to anneal the sample heating location and adjust the upstream and downstream laser powers to achieve similar CCD readout temperatures on both sides and a uniformly heated sample. A high-statistical quality SMS time spectrum is collected at the elevated annealing temperature in order to constrain a starting effective thickness of the sample heating location (Zhang et al., 2016). We refrained from collecting XRD images at high temperatures due to requisite long XRD exposure times.

Each heating run consists of a computer-controlled acquisition sequence, in which every 3 seconds the laser power is ramped up incrementally and various parameters are recorded, including the laser power, the time-integrated Mössbauer signal intensity (delayed counts), x-ray intensities from the ionization chambers, and temperature readouts from the FasTeR system and CCD spectrometer. The FasTeR system measures the downstream sample temperature and is characterized by a high sampling frequency,

recording $\sim$300 samplings for every 3 second interval, while the CCD-based spectrometer measures the upstream and downstream temperatures and performs one measurement at the start of every 3 second interval. The total time for each heating run is around 2 to 4 minutes following the start of the acquisition sequence. Once the heating run is completed, laser power is quenched, and an SMS spectrum is collected, followed by an XRD image.

2.3.2. X-ray diffraction

The XRD experiments are conducted at beamline 13-ID-D of the Advanced Photon Source, using a Pilatus CdTe 1M x-ray detector and incident x-rays of energy 37 keV focused to a spot size of $\sim$3x3 μm^2, measured by knife-edge scans using tungsten rods. A LaB$_6$ standard is used to calibrate the sample and image plate geometry. Double-sided infrared lasers produce a flat-top heating spot with diameter $\sim$10 μm (Prakapenka et al., 2008). Temperatures are measured on the upstream and downstream sides of the sample using a PIMAX 3 detector (Princeton Instruments) that records 1 to 10 measurements for every 4 second x-ray exposure window, with exposure time and measurement frequency adjusted for varying emission intensity. X-ray induced fluorescence on the sample is used to align the x-ray beam with the location of the laser heating spot and temperature measurements. Sample heating locations are annealed for at least 5 minutes at $\sim$1500 K.

For most XRD measurements, we use a burst heating method that involves alternating pairs of high-temperature ("hot") and quenched ("cold") measurements. The laser power is set to an initial low power to begin each heating run at a sample temperature of $\sim$1200 K. Laser shutters open to heat the sample and a 4 second "hot" XRD collection is triggered. Laser shutters are then immediately closed to quench the sample, and an ambient temperature "cold" XRD measurement is immediately collected, also for 4 seconds. Once a measurement pair is recorded, the laser power is increased to the next step in order to target a higher temperature for the next XRD measurement pair. Laser powers are adjusted to maintain upstream and downstream temperature balance and minimize axial thermal gradients in the sample. The total heating time for a single heating location is around 1 to 4 minutes, spread over the series of intermittent laser bursts. The short durations of continuous heating time in burst mode help to minimize hotspot drift and improve precision on x-ray and hotspot alignment. We additionally conduct two heating runs using a continuous heating method where laser power is manually increased during heating without intermittent quenching in an otherwise identical procedure that also uses 4 second XRD exposure times.

3. Results

3.1. Determination of the hcp – fcc phase boundary

X-ray diffraction images are integrated using the software DIOPTAS (Prescher and Prakapenka, 2015). All 300 K patterns confirm the presence of *hcp*-Fe$_{0.8}$Ni$_{0.1}$Si$_{0.1}$ and *B*2-KCl at ambient temperature, while high-temperature patterns reveal the transformation of the sample to *fcc* symmetry (Fig. 1a). Some ambient temperature patterns show remnant *fcc* reflections from crystal grains that do not transform back to the *hcp* phase during the rapid laser quench (Figs. 1b, 2c). The sluggish nature of this back-transformation has been previously observed for iron alloys (Komabayashi et al., 2012, 2019a). Additionally, some high-temperature patterns exhibit small remnant *hcp* peaks that persist after the bulk sample has transformed to the *fcc* phase, likely stemming from the radial tails of the x-ray beam that traverse colder parts of the sample. No other phases are identified from the patterns, suggesting no evidence of carbon contamination or other chemical reactions within detection limits. The temperatures used
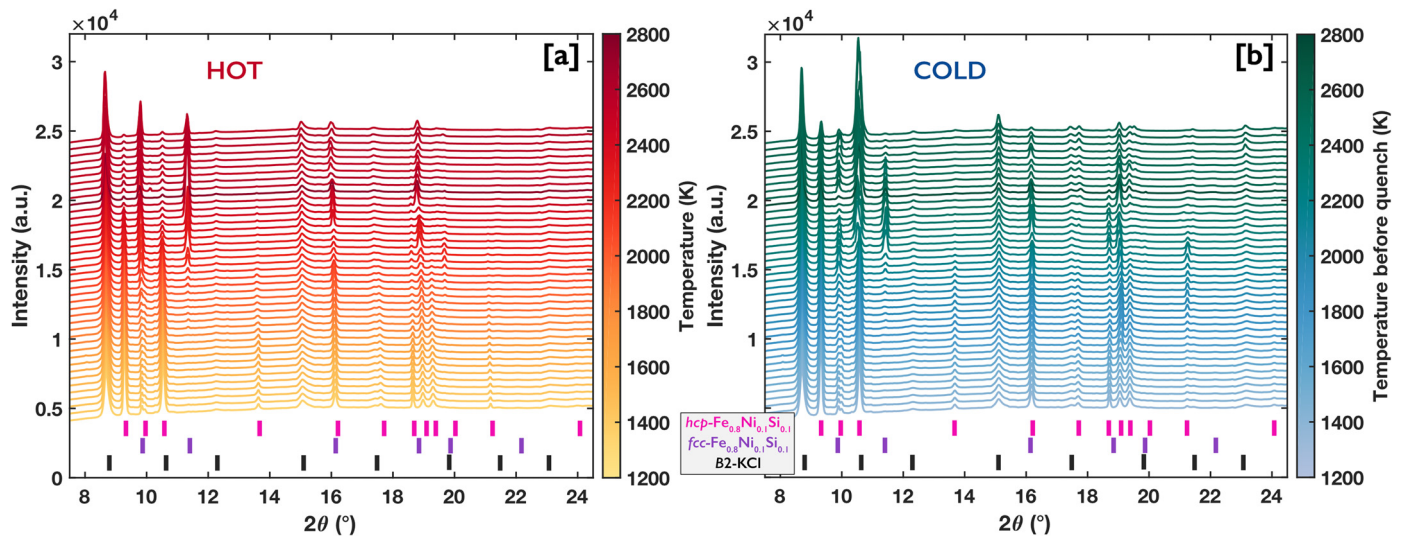
Fig. 1. High temperature ("hot") [a] and quenched ("cold") [b] integrated XRD patterns from burst heating run D1P2S3 (49-56 GPa), color-coded by temperature. Colored ticks below patterns identify reflections from hcp-$Fe_{0.8}Ni_{0.1}Si_{0.1}$ (pink), fcc-$Fe_{0.8}Ni_{0.1}Si_{0.1}$ (purple), and KCl (black). The sluggish fcc to hcp back-reaction can result in reflections from remnant fcc grains in patterns quenched from temperatures above the hcp-fcc transition (see also Fig. 2). (For interpretation of the colors in the figure(s), the reader is referred to the web version of this article.)
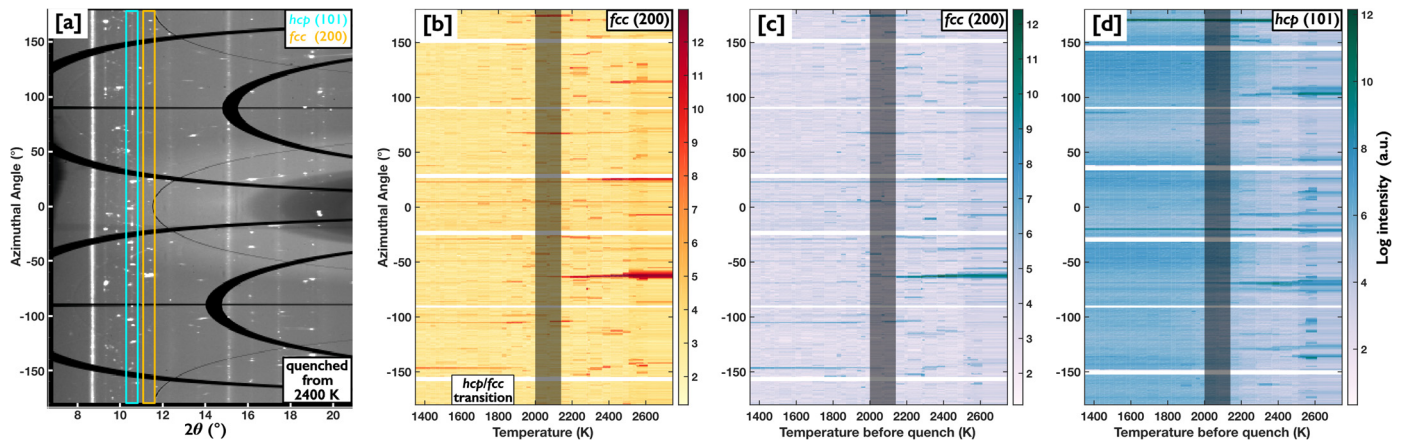

Fig. 2. Evolution of sample grain growth and recrystallization (texture) during heating run D1P2S3 (49-56 GPa). Panel [a] shows a raw 2D XRD image for a 300 K measurement quenched from 2400 K. Panels [b] and [c] show hot and cold azimuthal intensities of the fcc (200) reflection (yellow box in [a]) as a function of sample temperature and temperature before quench, respectively. Hot measurements ([b]) show grain growth and recrystallization of the fcc phase above the hcp-fcc transition (gray bar). Quenched measurements ([c]) capture "snapshots" of recrystallization effects due to the sluggish back transformation from fcc to hcp during rapid quench. Panel [d] shows 300 K intensities of the hcp (101) reflection (cyan bar in [a]). Texture of the quenched hcp phase evolves from fine-grained to coarse-grained as the sample is heated above the hcp-fcc transition.

for further analysis of the high-temperature patterns are the mean of the upstream and downstream temperatures, with uncertainties represented by the standard error of the mean. The dependence of sample temperature on the incident laser power cannot be reliably used to identify the onset of melting in this study (see Text S2, Fig. S1).

For all heating runs, we observe smooth continuous diffraction rings for high temperature hcp reflections and spotty diffraction rings for high temperature fcc reflections, as well as for remnant fcc reflections in quenched measurements (Fig. 2b-c, Movie S1). We interpret these observations as the onset of grain growth (texture development) concurrent with the hcp-fcc transition. With subsequent heating at temperatures above the transition, we observe changes in diffraction spot positions and in fcc reflection intensities (Fig. 3) with each heating step and XRD measurement, which we interpret as recrystallization of the fcc phase at high temperatures. We observe similar behavior during burst heating mode in the quenched hcp reflections, which transition from continuous to spotty diffraction rings (grain growth) (Fig. 2d) at the hcp-fcc tran-

sition and similarly exhibit changes in diffraction spot positions (recrystallization) with subsequent heating steps.

We constrain the temperature of the hcp-fcc phase boundary using multiple non-overlapping sample reflections from the high-temperature XRD patterns, choosing two to five individual reflections from both phases for all heating runs (listed in Figs. 3, S2-10). We integrate reflection intensities, subtract the integrated background intensity at each reflection, and normalize by the starting intensity. This procedure collapses all reflection intensities onto the same range of arbitrary intensity units, allowing for direct comparison and simultaneous fitting of all selected reflections for each phase. The loss of the hcp reflection intensities with increasing temperature is fit using a sigmoid function, whose finite width, generally ~400 K (Fig. 3, Figs. S2-10), results from two phenomena. A coexistence region (~100-200 K) is expected for the hcp and fcc phases, as observed previously for iron-silicon alloys (e.g., Komabayashi et al., 2019a). However, the likely presence of an axial temperature gradient in the sample (e.g., Sinmyo et al., 2019) could lead to overestimation of an hcp-out temperature, due to the
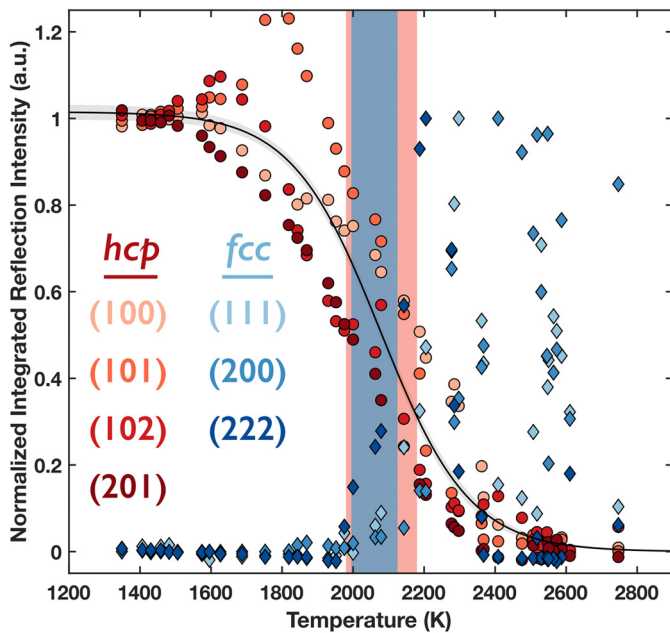
Fig. 3. Changes in normalized integrated intensities from multiple *hcp*- and *fcc*-$Fe_{0.8}Ni_{0.1}Si_{0.1}$ reflections during heating run D1P2S3 (49-56 GPa). Transition temperature is calculated as an average of *hcp-out* (red bar) and *fcc-in* (blue bar) temperatures. Recrystallization of *fcc* grains (Fig. 2) produces fluctuations in *fcc* reflection intensities.

presence of the *hcp* phase in the cooler sample interior even as the hotter sample surface has fully transformed to the *fcc* phase. To account for these effects, we calculate the *hcp-out* temperature as the 50% intensity value from the sigmoid fit, with uncertainty estimated from the scatter of individual reflection intensities around the sigmoid fit. The onset of *fcc* reflections with increasing temperature is not fit due to significant scatter in intensities, resulting from recrystallization of the *fcc* phase. Instead, the *fcc-in* temperature is estimated at around 20% of the maximum intensities with reasonable uncertainty. The temperature of the phase boundary is calculated as an average of the *hcp-out* and *fcc-in* temperatures, with total uncertainty as the root-mean-square of the difference in these temperatures and their individual uncertainties.

3.2. Detection of melting

3.2.1. Synchrotron Mössbauer spectroscopy

Determining the melting temperature of $Fe_{0.8}Ni_{0.1}Si_{0.1}$ from SMS experiments involves fitting the intensity of the Mössbauer signal as a function of the sample temperature, calculated as an average of the upstream and downstream CCD temperatures. We additionally bin the high-frequency FasTeR temperatures to match the 3 second measurement intervals of the CCD temperatures and SMS intensities. The standard deviation of the FasTeR temperatures within each 3 second interval provides a higher temporal estimate of the sample temperature fluctuations (averaging around 30-50 K) than the CCD measurements. Temperature uncertainties are calculated as a quadrature sum of the upstream and downstream CCD temperature difference and the FasTeR temperature fluctuations. FasTeR temperatures show excellent agreement with the downstream CCD temperatures during all heating runs.

We use the CONUSS software package (Sturhahn, 2000) to fit the high-temperature SMS time spectrum collected before the start of the acquisition sequence in order to constrain the effective thickness of the sample at the start of the heating run (Fig. 4a). Effective thickness is dimensionless and is the product of the numerical density of the ^{57}Fe atoms, the physical thickness of the sample, the nuclear resonant cross-section (2.56×10^{-22} m^2 for ^{57}Fe),

and the Lamb-Mössbauer factor (probability of recoil-free scattering events). We then calculate the Mössbauer signal intensity for each 3 second collection interval of the heating run (Fig. 4b) as the integral of delayed counts over the timing window. We normalize integrated counts by the x-ray intensity ratio measured by the upstream and downstream ionization chambers, in order to remove the effects of fluctuations in incident x-ray intensity and changes in the sample chamber thickness. Changes in the sample chamber thickness, as measured by the upstream and downstream ionization chambers, never exceed 2% for any heating runs (Figs. S11-14).

The starting effective thickness, along with the sizes and shapes of the x-ray beam and laser hot spot incident on the sample surface, are inputs into the MINUTI software SIMX module (Sturhahn, 2021), which models the temperature evolution of the normalized delayed counts as a function of temperature and fits the measured data to constrain the melting temperature (Fig. 4c) (see Zhang et al., 2016). We illustrate the effects of x-ray beam size and starting thickness on the Mössbauer intensity profiles as a function of temperature in a series of forward models (Fig. S15). We additionally show effects of a small offset between the x-ray beam and the laser hotspot, which is a fit parameter in all heating runs (reported in Table S1) and is in good agreement with offset magnitudes visually estimated with CCD cameras during heating. By incorporating experiment-specific details with an underlying physical basis for the temperature evolution of scattering events, this approach provides a meaningful and quantitative basis for interpreting the presence of melt.

3.2.2. X-ray diffuse scattering

Melting is revealed in XRD measurements by a liquid diffuse scattering signal, whose intensity must overcome a relatively large baseline background to be statistically detectable and may be difficult to identify solely from visual inspection of diffraction patterns. To quantify background intensity changes, we select a narrow background near the lowest 2θ sample reflections (Fig. 5a, c), an area relatively isolated from Bragg reflections and consistently shown to produce the strongest diffuse signal (e.g., Anzellini et al., 2013), and integrate this region for both the "hot" high-temperature and "cold" quenched patterns (Fig. 5b). The cold patterns in burst heating mode produce "snapshots" of the baseline reference background shape as it evolves during heating. Most heating runs exhibit noisy fluctuations in the reference background, likely caused by recrystallization above the *hcp-fcc* transition, that lead to the diffuse signal being difficult or impossible to detect in the hot patterns (Figs. S2-8) (e.g., Asanuma et al., 2010). The two continuous heating runs similarly exhibit background fluctuations and no obvious diffuse signal, indicating that the effect of recrystallization on background intensities is independent of heating mode (Figs. S9-10). Background fluctuations behave differently at different reflection angles (Fig. 5b), making it difficult to detect a diffuse signal by only comparing hot intensities at different angles.

We introduce a background updating method to quantify changes in the reference background level and facilitate the determination of the liquid diffuse signal onset. This method involves normalizing each hot intensity by the corresponding cold intensity, essentially updating the shape of the reference background with each heating step and removing the noisy fluctuations caused by recrystallization (Fig. 5d). For all burst heating runs, this procedure reveals the onset of a statistically significant discontinuous increase in background intensity that we interpret as the onset of a liquid diffuse signal. The gentle increase in background intensity before melting may be attributed to thermal diffuse scattering of the solid sample. We explore the effect of integrating different background regions, including fits to full 2θ backgrounds (Text S3, Figs. S16-17), and find that the strongest sensitivity to a liquid dif-
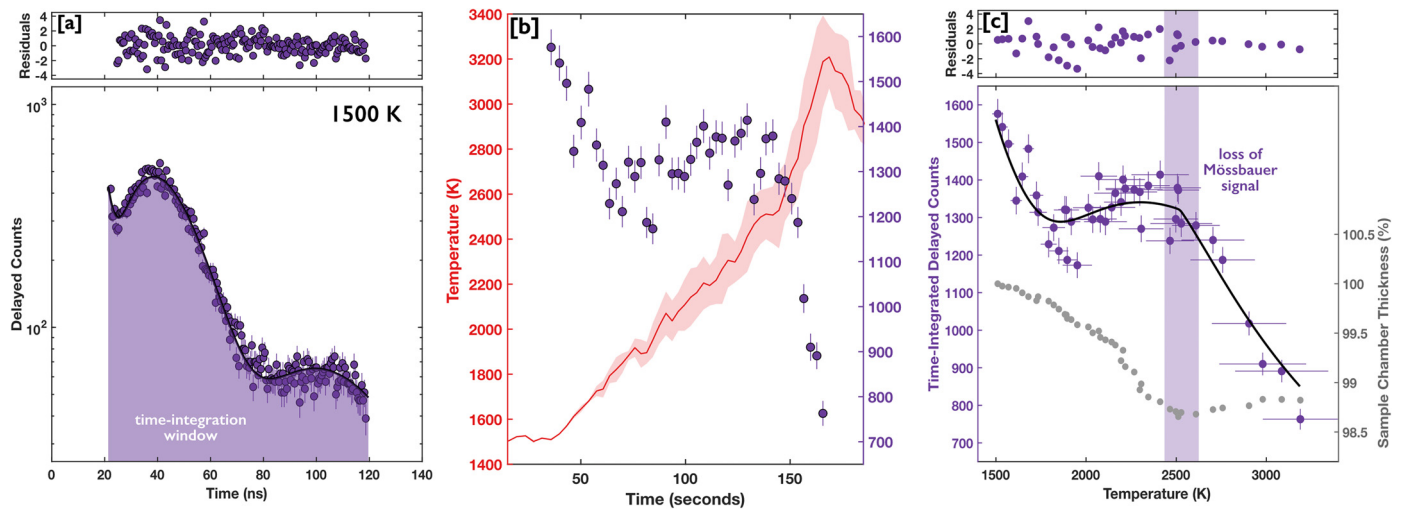
Fig. 4. Typical SMS measurement of melting (heating run D1S1, 43–47 GPa). Panel [a]: High-statistical quality Mössbauer time spectrum is collected for ∼5 minutes while annealing at ∼1500 K. Spectra are fit with CONUSS (Sturhahn, 2000) to calculate the sample starting thickness. Panel [b]: Temperature (red line, left axis) and time-integrated delayed counts (purple shading in [a]) are collected over a series of 3-second intervals as laser power is gradually increased in an automatic acquisition sequence. Sudden drop-off in counts occurs at the onset of melting. Panel [c]: Scattering intensity model (solid black line) is fit to the count-temperature profile (purple points, left axis) in MINUTI (Sturhahn, 2021) to constrain the melting temperature (purple bar). Changes in sample chamber thickness (gray points, right axis) are calculated from total x-ray transmission intensity changes and are limited to less than 2% for all heating runs. Residuals from the fits are shown in units of standard deviation.
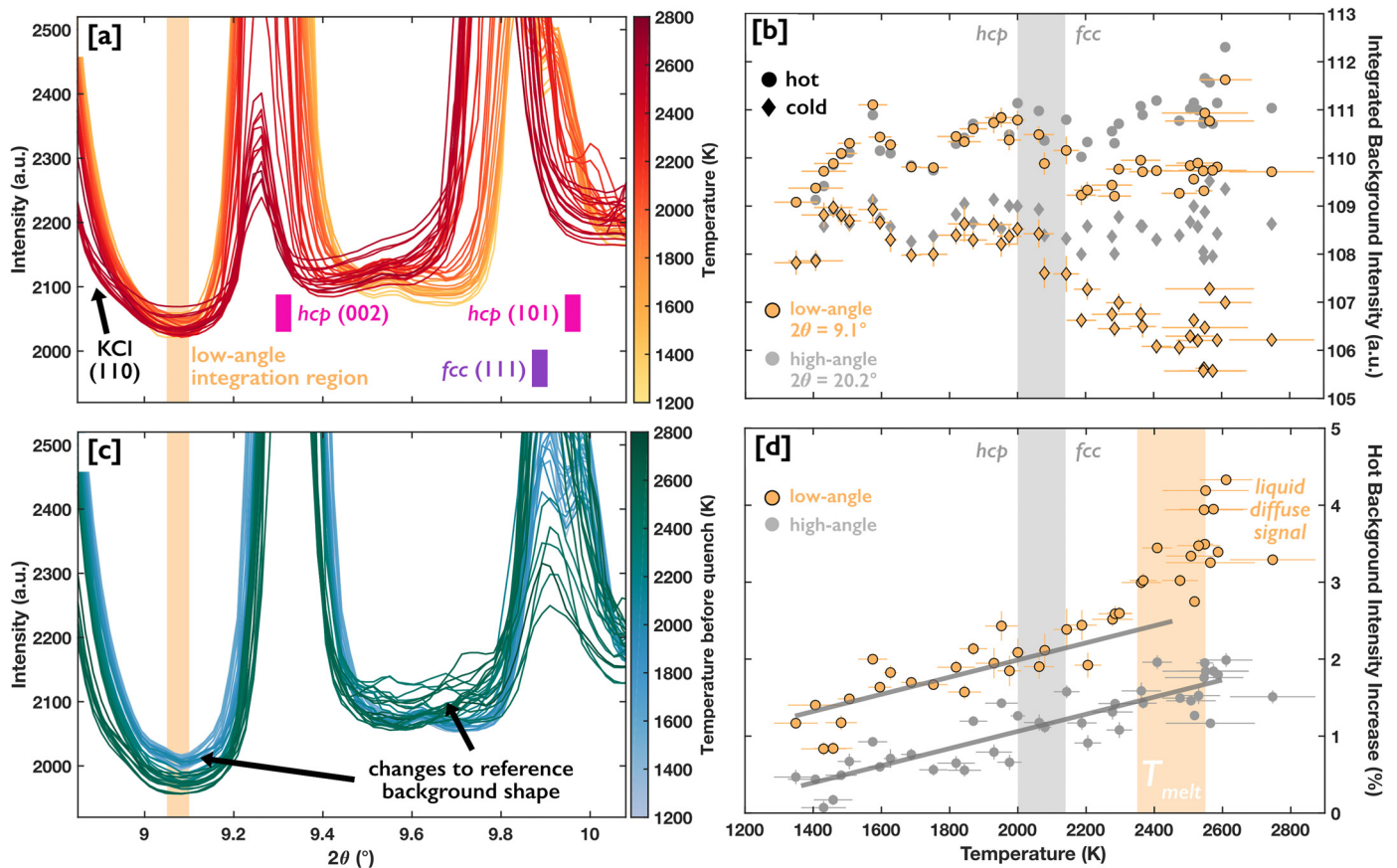

Fig. 5. Background intensity analysis for heating run D1P2S3 (49–56 GPa). Panels [a] and [c] show high temperature ("hot") and quenched ("cold") integrated XRD patterns, respectively, in the region expected to exhibit the strongest liquid diffuse scattering signal. Quenched patterns show noisy fluctuations in the reference background shape, especially above the *hcp-fcc* transition (2070 ± 70 K) due to recrystallization of the sample. Low-angle integration region (orange bar) is selected due to relative isolation from reflections and smaller fluctuations due to recrystallization. Panel [b] shows integrated intensities at low-angle (orange) and high-angle (gray) regions for both hot (circle) and cold (diamond) patterns. Shaded gray bar represents the *hcp-fcc* transition. Panel [d] shows normalized hot background intensities after the background updating procedure (Section 3.2.2) that reveals a liquid diffuse scattering signal from the melt and allows for constraining the melting temperature (shaded orange bar). Gray lines are guides for the eye to demonstrate the presence and absence of the diffuse signal at the low-angle (orange) and high-angle (gray) regions, respectively.
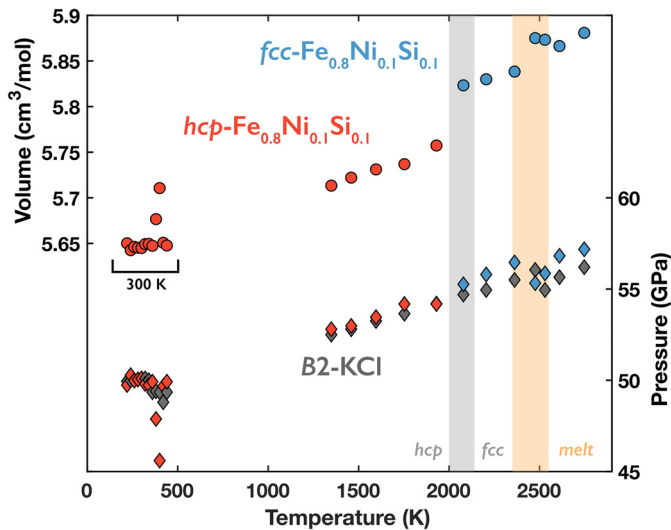
Fig. 6. Unit-cell volumes and pressures for burst heating run D1P2S3. Volumes (left y-axis, circles) for *hcp*- (red) and *fcc*-$Fe_{0.8}Ni_{0.1}Si_{0.1}$ (blue) are constrained from fits to integrated XRD patterns using GSAS-II (Toby and Von Dreele, 2013). *In-situ* pressures (right y-axis, diamonds) for the sample and the KCl pressure medium (gray) are calculated from volumes using previously published thermal equations of state (see Section 3.3). 300 K measurement results are spaced out for ease of viewing in the order of acquisition sequence, from first (leftmost) to last (rightmost) heat and quench step. Onset of a plateau in volumes aligns with the melting temperature determined from the liquid diffuse scattering signal (orange bar). The shaded gray bar represents the *hcp-fcc* transition.

fuse signal is achieved with integration of the narrow low-angle region and use of the reference background updating method.

3.2.3. Unit-cell volumes

Lattice parameters and unit cell volumes for $Fe_{0.8}Ni_{0.1}Si_{0.1}$ and KCl phases are determined from fits of the XRD patterns using the GSAS-II software package (Toby and Von Dreele, 2013) for a sampling of measurements from each heating run (Fig. 6). For most runs, the melting temperature as determined by the liquid diffuse scattering signal seems to generally align with the onset of a volume plateau (Anzellini et al., 2013), though scatter in the volume data poses a challenge to place precise constraints on the melting temperature. For the two continuous heating runs, where no diffuse signal can be detected, we can estimate a melting temperature from the onset of a volume plateau (Figs. S9-10). We additionally calculate c/a ratios of the *hcp* phase for all measurements (Fig. S18) and find excellent agreement with previous reports (Morrison et al., 2018; Komabayashi et al., 2019b).

3.3. In-situ pressure determination and thermal pressure calculation

Previously published thermal equations of state (Tateno et al., 2019; Morrison et al., 2018; Komabayashi et al., 2019b; Edmund et al., 2020; Komabayashi, 2014) are used to calculate *in-situ* pressures of *B2*-KCl, *hcp*-$Fe_{0.8}Ni_{0.1}Si_{0.1}$, and *fcc*-$Fe_{0.8}Ni_{0.1}Si_{0.1}$ for high-temperature and quenched XRD measurements (Table S2 and Text S4). These equations of state result in excellent agreement between $Fe_{0.8}Ni_{0.1}Si_{0.1}$ and KCl pressures, consistently within 1-2 GPa, for both ambient and high temperatures (Fig. 6), though *fcc* pressures exhibit more scatter likely due to recrystallization effects. Final XRD pressures used for phase boundary location are an average of $Fe_{0.8}Ni_{0.1}Si_{0.1}$ and KCl pressures, with uncertainties calculated as the difference in pressures.

Using the *in-situ* pressures calculated for the XRD measurements, we can constrain the thermal contribution to pressures in the sample chamber as a function of temperature. We calculate thermal pressures of the $Fe_{0.8}Ni_{0.1}Si_{0.1}$ sample by compiling all
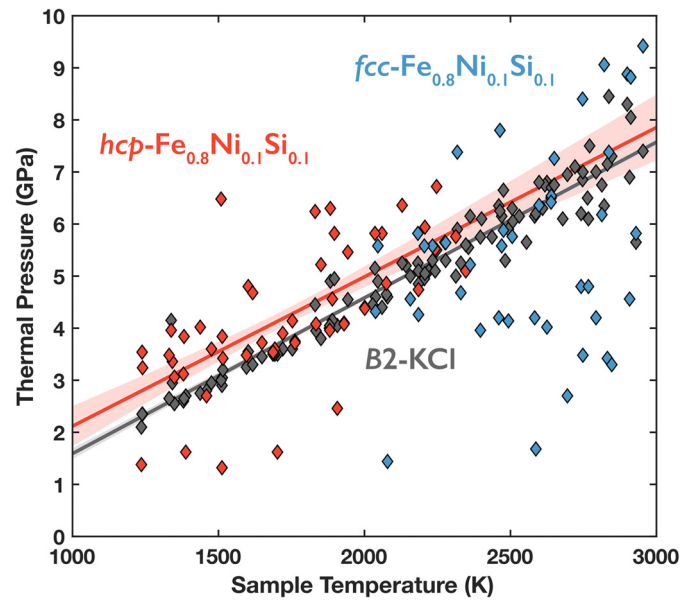

Fig. 7. Compilation of all thermal pressures of all XRD measurements in this study, calculated as the difference between hot and corresponding quenched cold pressures, for *hcp*- (red) and *fcc*-$Fe_{0.8}Ni_{0.1}Si_{0.1}$ (blue) and *B2*-KCl (gray). Linear fits of thermal pressure slopes (solid lines) for *hcp*-$Fe_{0.8}Ni_{0.1}Si_{0.1}$ [2.9±0.9 GPa per 1000 K] and *B2*-KCl [2.9±0.1 GPa per 1000 K] show excellent agreement. Onset of scatter in pressure for the *fcc* phase corresponds to the onset of melting in the XRD measurements. For further details on the thermal pressure model constructed from these data, see Section 3.3, Text S5, and Figs. S19-21.

hot pressure increases relative to pressures of the corresponding quenched measurement. A linear fit to all sample thermal pressures constrains a slope of 2.9±0.9 GPa per 1000 K, in excellent agreement with the fit to all KCl thermal pressures (2.9±0.1 GPa per 1000 K) (Fig. 7). Based on these *in-situ* measurements, we report a thermal pressure model for $Fe_{0.8}Ni_{0.1}Si_{0.1}$ in a KCl pressure medium: 2.9 GPa per 1000 K with an added uncertainty of 3 GPa on pressures at melting. This thermal pressure model accounts for uncertainties in KCl temperatures, while showing agreement with published *in-situ* measurements on Fe and $Fe_{0.9}Ni_{0.1}$ in a KCl pressure medium (see Text S5 and Figs. S20-21 for details). We apply this thermal pressure model to all SMS measurements in this study, with starting cold pressures calculated from the XRD measurements taken before and after each SMS heating run.

3.4. Phase diagram of $Fe_{0.8}Ni_{0.1}Si_{0.1}$

We present a summary of all measurements conducted in this study in Fig. 8, spanning a range from 20 to 83 GPa and 1200 to 3500 K, with *P-T* conditions of measured phase boundaries reported in Table S1. Melting temperatures demonstrate both strong reproducibility for each individual melt detection technique as well as excellent agreement within mutual uncertainties between the two independent techniques. We calculate a fit to all melting points with the commonly used empirical Simon-Glatzel formulation (Simon and Glatzel, 1929)

$$T_m = T_{m0} \left(\frac{P_m - P_{m0}}{x} + 1 \right)^y$$

where the melting points (T_m, P_m) are related to a reference melting point (T_{m0}, P_{m0}) and x, y are adjustable, material-specific fit parameters. For $Fe_{0.8}Ni_{0.1}Si_{0.1}$, we find best-fit values $T_{m0} = 1990\pm50$ K, $P_{m0} = 23\pm1$ GPa, $x = 10\pm5$ GPa, and $y = 0.18\pm0.05$, resulting in the melting curve shown in Fig. 8 with fit quality $R^2 = 0.92$. For the *hcp-fcc* boundary, we calculate a linear fit with
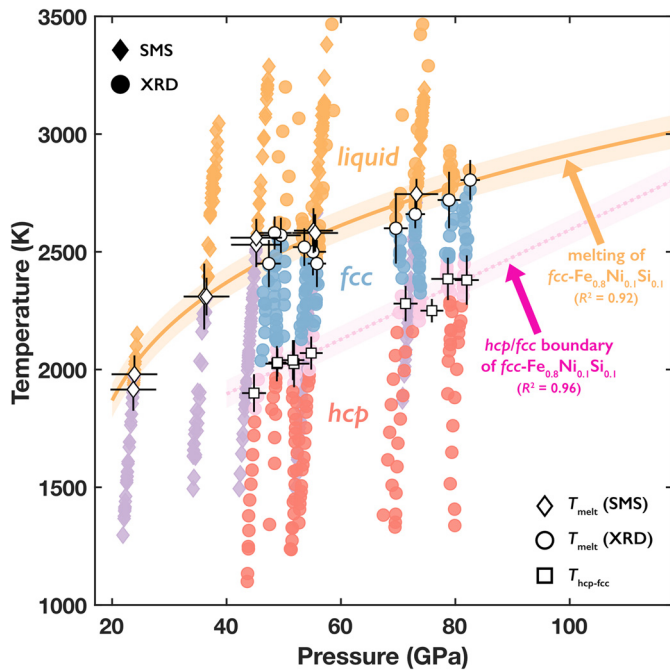
Fig. 8. Compilation of pressure, temperature, and phase conditions of all measurements (color points) in this study for SMS (diamonds) and XRD (circles) heating runs. White points represent phase boundaries as determined in Sections 3.1 and 3.2 (reported in Table S1). Melting temperatures from SMS and XRD techniques exhibit excellent agreement and reproducibility within uncertainties: liquid (orange), solid (purple, SMS; blue, XRD). XRD runs additionally constrain the solid *hcp-fcc* transition (*hcp* – red, *fcc* – blue, transition range – pink). Solid lines are fits to phase boundaries with shaded uncertainties. See Section 3.4 and Text S6 for fitting details.

slope 11.6±0.9 K/GPa and 0 GPa intercept 1430±55 K, resulting in the phase boundary shown in Fig. 8 with $R^2 = 0.96$. The intersection of these two phase boundaries is calculated to constrain the location of the *hcp-fcc-liquid* quasi-triple point at 147±14 GPa and 3140±90 K. In reality, melting of an alloy should be described by a solidus and liquidus. Within our experimental resolution however, the solidus and liquidus are indistinguishable and are addressed simply as the melting curve of $Fe_{0.8}Ni_{0.1}Si_{0.1}$, in accordance with previous studies on Fe-Ni and Fe-Si systems (e.g., Asanuma et al., 2010; Zhang et al., 2016). Treatment of uncertainties and error propagation is discussed in Text S6.

4. Discussion

4.1. Comparison with previous studies

In order to compare with previous studies and discuss the effects of silicon on the melting temperatures of Fe and Fe-Ni, we first conduct a systematic analysis to determine the relative effects from similar measurements. To do so, we apply our new thermal pressure model to previous SMS melting data on Fe and $Fe_{0.9}Ni_{0.1}$ (Jackson et al., 2013; Zhang et al., 2016), which were collected at the same beamline using identical experimental techniques as this study. Using these recalculated pressures, we fit updated SMS melting curves for *fcc*-Fe and *fcc*-$Fe_{0.9}Ni_{0.1}$ (Fig. 9, Text S7). We now consider how the recalculated SMS data on Fe and $Fe_{0.9}Ni_{0.1}$ compare with other recent melting studies and find that discrepancies remain.

We therefore examine a recently proposed hypothesis (Morard et al., 2018) suggesting that differences in pressure metrology alone explain discrepancies in *fcc*-Fe melting temperatures among various techniques. To do so, we compile recent measurements of Fe melting from a range of *in-situ* techniques (Fig. 9a). The highest melting temperatures are from Anzellini et al. (2013) and Hou et

al. (2021), while the lowest are reported by Aquilanti et al. (2015), Sinmyo et al. (2019), and Basu et al. (2020), spanning a range of ~700 K at 100 GPa. SMS results (Jackson et al., 2013; Zhang et al., 2016), fall in between these two bounds and are generally compatible with Sinmyo et al. (2019) and Basu et al. (2020) within mutual uncertainties. Results from Boehler et al. (2008) are in excellent agreement with SMS results, while results from Morard et al. (2018) display better agreement with lower bound temperatures at lower pressures and general agreement with upper bound temperatures at higher pressures. This compilation shows disagreements among studies that are significantly larger than measurement uncertainties. Important for the discussion here, Anzellini et al. (2013) and Sinmyo et al. (2019) report nearly identical thermal pressures (Figs. S20-21, Text S5), while displaying up to 700 K difference in melting temperatures.

The above comparisons suggest that pressure metrology alone cannot resolve discrepancies in *fcc*-Fe melting data. They also cannot necessarily be attributed to the specific *in-situ* diagnostics used to determine the onset of melting. This can be seen from the fact that similar diagnostic methods for melt detection, such as sample resistivity (Sinmyo et al., 2019; Basu et al., 2020; Hou et al., 2021), changes in x-ray absorption spectra (XAS) (Aquilanti et al., 2015; Morard et al., 2018), and appearance of a liquid diffuse x-ray scattering signal (XRD) (Boehler et al., 2008; Anzellini et al., 2013), have all given results at both the upper and lower temperature bounds (Fig. 9a). Our study examines independent experimental datasets, from XRD with a background updating method and from SMS, finding excellent agreement in melting temperatures. Therefore, identical diagnostic methods may still involve different interpretations of the onset of melting.

The apparent discrepancies may also result from other experimental factors. One possibility is carbon contamination from the diamond anvils (Prakapenka et al., 2003), which could lead to underestimated melting temperatures due to the formation and melting of Fe_3C, as suggested by Morard et al. (2018). However, this explanation is difficult to apply to the measurements of Boehler et al. (2008) and Sinmyo et al. (2019), both of whom observed the loss of Fe reflections upon melting and no Fe_3C reflections in their XRD data. Another possibility is variable thickness of samples and differing heating methods (one-sided or two-sided laser heating, and electrical heating), which could produce temperature gradients in the sample and potentially lead to overestimated melting temperatures, as suggested by Sinmyo et al. (2019). However, such axial temperature gradients are unlikely to be larger than ~250 K for typical sample thicknesses (~5 μm) and would be negligible for thin samples (~1 μm) (Sinmyo et al., 2019). Another factor could involve temperature determination from Planck fits of thermal emission spectra, which could lead to both overestimation and underestimation of melting temperatures, as suggested by Hou et al. (2021). We note that the temperature measurement system at beamline 3-ID-B (APS) was calibrated using the temperature asymmetry of the NRIXS spectra (Lin et al., 2004; Sturhahn and Jackson, 2007), which is independent of the optical path. Aquilanti et al. (2015) also suggested that misalignments of the x-ray beam and laser hotspot could lead to overestimation of melting temperatures.

For Fe-Ni, results from Torchio et al. (2020) on the melting of *fcc*-$Fe_{0.8}Ni_{0.2}$ using x-ray absorption spectroscopy (XAS) show systematically higher temperatures than SMS results on *fcc*-$Fe_{0.9}Ni_{0.1}$ (Zhang et al., 2016), but are compatible within mutual reported uncertainties, spanning a range of ~300 K at 100 GPa (Fig. 9b), and both studies reach similar conclusions. Specifically, when comparing with XAS results on Fe (Morard et al., 2018), Torchio et al. (2020) found negligible effect of nickel on melting temperatures, in excellent agreement with the relative effect of nickel determined by SMS measurements (Zhang et al., 2016). These conclusions lend confidence that the relative effect of alloyed-Ni and
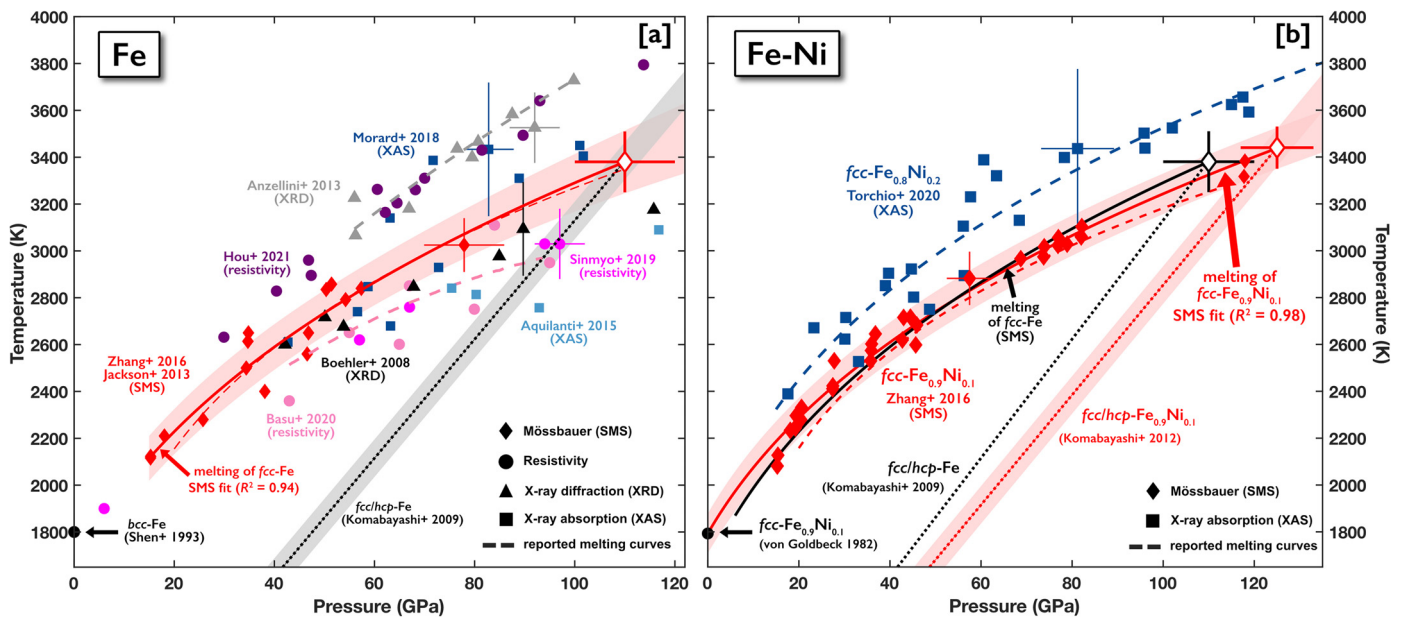
Fig. 9. Melting points from a variety of experimental techniques. Panel [a]: melting of Fe as measured by SMS (red – pressures recalculated from Jackson et al., 2013 and Zhang et al., 2016), resistivity changes (dark purple – Hou et al., 2021; magenta – Sinmyo et al., 2019; light pink – Basu et al., 2020), XAS (dark blue – Morard et al., 2018; light blue – Aquilanti et al., 2015), and XRD without burst heating and background updating (gray – Anzellini et al., 2013; black – Boehler et al., 2008). Representative uncertainties are shown for one data point from each study. An updated melting curve for *fcc*-Fe (solid red line) is fit to the SMS data. The *hcp-fcc-liquid* triple point (open red diamond) is calculated from the intersection of the melting curve with the previously determined *hcp-fcc* boundary (dotted line - Komabayashi et al., 2009). Previously reported melting curves are shown with dashed lines (red – Zhang et al., 2016, pink – Basu et al., 2020, gray – Anzellini et al., 2013). The 0 GPa melting point for *bcc*-Fe is taken from Shen et al. (1993). Panel [b]: melting of *fcc*-Fe$_{0.9}$Ni$_{0.1}$ as measured by SMS (red – pressures recalculated from Zhang et al., 2016) and of *fcc*-Fe$_{0.8}$Ni$_{0.2}$ as measured by XAS (dark blue – Torchio et al., 2020). An updated melting curve for *fcc*-Fe$_{0.9}$Ni$_{0.1}$ is shown with the solid red line. The *hcp-fcc-liquid* quasi-triple point (open red diamond) is calculated from the intersection of the melting curve with the previously determined *hcp-fcc* boundary (dotted red line – Komabayashi et al., 2012). The 0 GPa melting point for *fcc*-Fe$_{0.9}$Ni$_{0.1}$ is taken from von Goldbeck (1982). See Section 4.1 and Text S7 for details.

Si on iron's melting curve can be well-constrained, despite open questions about the accuracy of various *fcc*-Fe melting curves.

4.2. Effect of nickel and silicon on phase relations in planetary cores

A recent compilation of melting studies on silicon-bearing iron alloys measured by XRD without burst heating and background updating (Fischer, 2016) illustrates the challenge of interpreting the effect of silicon on the melting temperatures of iron due to sparsity and scatter of data (reproduced in Fig. 10). When compared to the melting curve of pure Fe measured by XRD (Anzellini et al., 2013), Fe$_{0.84}$Si$_{0.16}$ (9wt%Si) shows a decrease in melting temperature below 50 GPa and a possible increase above 90 GPa (Fischer et al., 2013), while Fe$_{0.74}$Si$_{0.27}$ (16wt%Si) shows a decrease of variable magnitude from 20 to 140 GPa (Fischer et al., 2012) and Fe$_{0.70}$Si$_{0.30}$ (18wt%Si) shows negligible effect below 60 GPa and a growing decrease from 60 to 120 GPa (Asanuma et al., 2010). For nickel-bearing compositions, the only prior static compression melting study on such alloys shows that the melting curves of Fe$_{0.78}$Ni$_{0.04}$Si$_{0.18}$ (10wt%Si) and Fe$_{0.70}$Ni$_{0.04}$Si$_{0.26}$ (15wt%Si) measured by XRD (Morard et al., 2011) exhibit lower temperatures and greater curvature relative to Fe (Anzellini et al., 2013). Two measurements of Fe$_{0.75}$Ni$_{0.07}$Si$_{0.18}$ (10wt%Si) from a shock compression study (Zhang et al., 2018) may be compatible with results from Morard et al. (2011), though the studied pressure ranges do not overlap, and significant uncertainty may exist in the thermal conductivity values used to model the measured raw interfacial temperatures. Importantly, no melting studies exist on alloys with more moderate concentrations of Si (<9wt%).

Interpretation is challenging in part because Fe crystallizes in the *fcc* structure from the melt below 100 GPa and *hcp* above 100 GPa, while alloys with relatively high Si concentration (≥ 9wt%) can exhibit phase mixtures like *B2* + *fcc* + *hcp* or the presence of *bcc*-like phases (Fischer et al., 2013; Asanuma et al., 2010; Wicks et

al., 2018). Morard et al. (2011) similarly observed a mix of *fcc* and *bcc* phases present at melting for Fe$_{0.78}$Ni$_{0.04}$Si$_{0.18}$ (10wt%Si) in the studied pressure range (20-80 GPa). In contrast, lower Si concentrations such as Fe$_{0.92}$Si$_{0.08}$ (4wt%Si) and Fe$_{0.88}$Si$_{0.12}$ (6.5wt%Si) have been shown to exhibit *fcc* and *hcp* stability fields similar to Fe, albeit with the *hcp-fcc* transition boundary shifted to higher temperatures (Komabayashi et al., 2019a). Komabayashi et al. (2019b) showed that Fe$_{0.88}$Ni$_{0.04}$Si$_{0.08}$ (4wt%Si) exhibits *fcc* and *hcp* stability fields similar to Fe but with a flatter transition boundary relative to Fe (Komabayashi et al., 2009) (Fig. 10), in agreement with an earlier study on Fe$_{0.88}$Ni$_{0.04}$Si$_{0.08}$ (4wt%Si) that observed the *hcp* phase at Earth's inner core conditions (Sakai et al., 2011).

Using the updated SMS melting curves of *fcc*-Fe and *fcc*-Fe$_{0.9}$Ni$_{0.1}$ calculated in Section 4.1, we systematically evaluate the effect of silicon. We find that the addition of 10 mol% Si reduces the melting temperature of Fe$_{0.9}$Ni$_{0.1}$ by ~250 K at low pressures (<60 GPa) and up to 500 K at conditions of Earth's outermost core (Fig. 10). These findings are in qualitative agreement with results from Morard et al. (2011), who found a similar reduction in temperature and increase in curvature of the melting boundary for Fe$_{0.70}$Ni$_{0.04}$Si$_{0.26}$ relative to pure Fe (Anzellini et al., 2013). While the relative effect is consistent, we note the systematically larger melting temperatures in these aforementioned XRD studies compared to results from this study. These offsets could be caused by several experimental factors discussed in Section 4.1 for pure Fe, some of which may explain the findings of Asanuma et al. (2010), who identified melting of Fe$_{0.70}$Si$_{0.30}$ from temperature discontinuities and recovered sample textures but could not detect liquid diffuse signals.

Regarding subsolidus phase relations, we find that Fe$_{0.8}$Ni$_{0.1}$Si$_{0.1}$ exhibits *fcc* and *hcp* stability fields similar to Fe but with a transition boundary featuring a much shallower slope and higher temperatures at low pressure. This combined effect of Ni and Si is in qualitative agreement with the previous study on Fe$_{0.88}$Ni$_{0.04}$Si$_{0.08}$
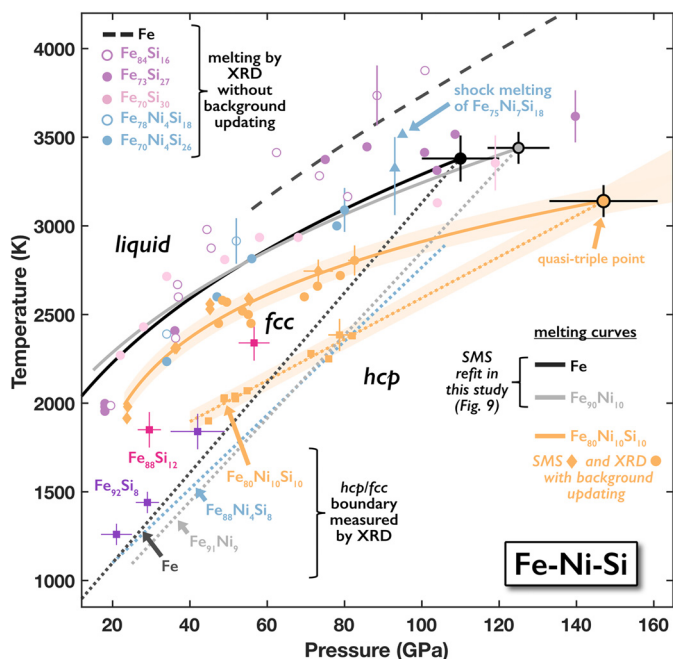
Fig. 10. Phase boundaries of $Fe_{80}Ni_{10}Si_{10}$ measured in this study (orange lines; see Fig. 8 for orange symbol shapes), with the calculated *hcp-fcc-liquid* quasi triple point (black outlined orange circle) and a Simon-Glatzel model for the melting curve (Text S7). Solid black and gray curves are SMS melting of Fe and $Fe_{90}Ni_{10}$, respectively, as refit in this study (Section 4.1, Fig. 9, Text S7). Dashed black line is the melting of Fe determined by XRD without burst heating and background updating (Anzellini et al., 2013). Dotted lines show the *hcp-fcc* boundary previously determined by XRD (in a resistive-heated DAC) for Fe (black, Komabayashi et al., 2009), $Fe_{91}Ni_9$ (gray, Komabayashi et al., 2012), and $Fe_{88}Ni_4Si_8$ (blue, Komabayashi et al., 2019b), while squares show the *hcp-fcc* boundary for $Fe_{92}Si_8$ (purple) and $Fe_{88}Si_{12}$ (pink) (Komabayashi et al., 2019a). Melting temperatures of Fe(-Ni)-Si from previous studies using XRD without burst heating and background updating (in a laser-heated DAC) are plotted as an average of reported lower and upper bounds (empty purple circles: Fischer et al., 2013; filled purple circles: Fischer et al., 2012; filled pink circles: Asanuma et al., 2010; blue circles: Morard et al., 2011). Shock melting of $Fe_{75}Ni_7Si_{18}$ is shown in blue triangles (Zhang et al., 2018), with an asymmetric error bar encompassing the raw interfacial temperature measurement value (-150 K) and uncertainty (121 K). Error bars are plotted for at least one representative data point for each melting study.

(Komabayashi et al., 2019b), with a more pronounced flattening effect on the boundary in this study due to greater concentrations of both Ni and Si. The reduction in melting temperatures and flattening of the *hcp-fcc* boundary leads to an *hcp-fcc-liquid* quasi-triple point for $Fe_{0.8}Ni_{0.1}Si_{0.1}$ at higher pressures and lower temperatures relative to Fe and Fe-Ni. The resulting melting temperature of $Fe_{0.8}Ni_{0.1}Si_{0.1}$ is 400 K lower than that of *fcc*-$Fe_{0.9}Ni_{0.1}$ at 125 GPa and 500 K lower than that of *hcp*-$Fe_{0.9}Ni_{0.1}$ at 150 GPa, if the *hcp*-$Fe_{0.9}Ni_{0.1}$ melting curve has the same shape as the *hcp*-Fe melting curve (Sinmyo et al., 2019).

5. Conclusion

In this study, we present a multi-technique approach for probing the dynamics and spatial positions of atoms in iron-bearing materials to measure solid phase relations and melting curves at extreme conditions. Specifically, we apply synchrotron Mössbauer spectroscopy and x-ray diffraction methods to $Fe_{0.8}Ni_{0.1}Si_{0.1}$, a composition compatible with recent estimates for the cores of Earth and Mercury, to clarify the combined effects of nickel and silicon on planetary cores. To our knowledge, this study represents the first combined use of these two techniques, sensitive to different atomic-level properties at different time and length scales, to detect melt. The introduction of a burst heating and background updating method for the XRD measurements leads to

excellent agreement in the melting temperatures determined independently by the two techniques. Using a thermal pressure model constructed in this study, we present updated SMS melting curves for *fcc*-Fe and *fcc*-$Fe_{0.9}Ni_{0.1}$ to systematically evaluate the relative effect of silicon.

We find that the addition of 10 mol% Si to $Fe_{0.9}Ni_{0.1}$ reduces melting temperatures by 250 K at low pressures (<60 GPa) and flattens the *hcp-fcc* boundary. These pressures are relevant to small terrestrial-type cores like in Mercury (<35 GPa), and if silicon is the major light element in Mercury's core, the lower melting temperatures imply lower core temperatures and/or a smaller inner core (Knibbe and van Westrenen, 2018). We find that silicon extends the *hcp-fcc-liquid* quasi-triple point of $Fe_{0.9}Ni_{0.1}$ to higher pressures and lower temperatures, resulting in a decrease in melting temperature at Earth's outermost core pressures by 500 K. If one assumes an identical curvature of the *hcp* melting boundary for $Fe_{0.8}Ni_{0.1}Si_{0.1}$ as for Fe (Zhang et al., 2016) and no effect on the shape of the core adiabat, then 10 mol% (5.3wt%) silicon would suggest that the core-side temperature of the core-mantle boundary (CMB) is around 3500 K. This temperature is below the lowest estimates for solidus temperatures of lower mantle assemblages at the CMB (Nomura et al., 2014) and lends support for solid-state interpretations of seismic heterogeneities like ultralow velocity zones (Wicks et al., 2017; Dobrosavljevic et al. 2019; Jackson and Thomas, 2021).

CRediT authorship contribution statement

Vasilije V. Dobrosavljevic: Conceptualization, Formal analysis, Investigation, Methodology, Software, Visualization, Writing – original draft, Writing – review & editing. **Dongzhou Zhang:** Investigation, Methodology, Software, Writing – review & editing. **Wolfgang Sturhahn:** Investigation, Software, Writing – review & editing. **Jiyong Zhao:** Methodology. **Thomas S. Toellner:** Methodology, Writing – review & editing. **Stella Chariton:** Methodology. **Vitali B. Prakapenka:** Methodology, Writing – review & editing. **Olivia S. Pardo:** Investigation, Writing – review & editing. **Jennifer M. Jackson:** Conceptualization, Funding acquisition, Investigation, Methodology, Project administration, Supervision, Writing – review & editing.

Declaration of competing interest

The authors declare that they have no known competing financial interests or personal relationships that could have appeared to influence the work reported in this paper.

Acknowledgements

Appendix A. Supplementary material

Supplementary material related to this article can be found online at https://doi.org/10.1016/j.epsl.2021.117358.

References

Anzellini, S., Dewaele, A., Mezouar, M., Loubeyre, P., Morard, G., 2013. Melting of iron at Earth's inner core boundary based on fast X-ray diffraction. Science 340 (6131), 464–466. https://doi.org/10.1126/science.1233514.

Aquilanti, G., Trapananti, A., Karandikar, A., Kantor, I., Marini, C., Mathon, O., Pascarelli, S., Boehler, R., 2015. Melting of iron determined by X-ray absorption spectroscopy to 100 GPa. Proc. Natl. Acad. Sci. 112 (39), 12042–12045. https://doi.org/10.1073/pnas.1502363112.

Asanuma, H., Ohtani, E., Sakai, T., Terasaki, H., Kamada, S., Kondo, T., Kikegawa, T., 2010. Melting of iron–silicon alloy up to the core–mantle boundary pressure: implications to the thermal structure of the Earth's core. Phys. Chem. Miner. 37 (6), 353–359. https://doi.org/10.1007/s00269-009-0338-7.

Basu, A., Field, M.R., McCulloch, D.G., Boehler, R., 2020. New measurement of melting and thermal conductivity of iron close to outer core conditions. Geosci. Front. 11 (2), 565–568. https://doi.org/10.1016/j.gsf.2019.06.007.

Boehler, R., Santamaría-Pérez, D., Errandonea, D., Mezouar, M., 2008. Melting, density, and anisotropy of iron at core conditions: new x-ray measurements to 150 GPa. J. Phys. Conf. Ser. 121 (2), 022018. https://doi.org/10.1088/1742-6596/121/2/022018.

Dannberg, J., Myhill, R., Gassmöller, R., Cottaar, S., 2021. The morphology, evolution and seismic visibility of partial melt at the core-mantle boundary: implications for ULVZs. Geophys. J. Int., 1028–1059. https://doi.org/10.1093/gji/ggab242.

Dobrosavljevic, V.V., Sturhahn, W., Jackson, J.M., 2019. Evaluating the role of iron-rich (Mg, Fe)O in ultralow velocity zones. Minerals 9 (12), 762. https://doi.org/10.3390/min9120762.

Edmund, E., Miozzi, F., Morard, G., Boulard, E., Clark, A., Decremps, F., Garbarino, G., Svitlyk, V., Mezouar, M., Antonangeli, D., 2020. Axial compressibility and thermal equation of state of Hcp Fe–5wt% Ni–5wt% Si. Minerals 10 (2), 98. https://doi.org/10.3390/min10020098.

Fischer, R.A., Campbell, A.J., Caracas, R., Reaman, D.M., Dera, P., Prakapenka, V.B., 2012. Equation of state and phase diagram of Fe–16Si alloy as a candidate component of Earth's core. Earth Planet. Sci. Lett. 357–358, 268–276. https://doi.org/10.1016/j.epsl.2012.09.022.

Fischer, R.A., Campbell, A.J., Reaman, D.M., Miller, N.A., Heinz, D.L., Dera, P., Prakapenka, V.B., 2013. Phase relations in the Fe–FeSi system at high pressures and temperatures. Earth Planet. Sci. Lett. 373, 54–64. https://doi.org/10.1016/j.epsl.2013.04.035.

Fischer, R.A., 2016. Melting of Fe alloys and the thermal structure of the core. In: Deep Earth. In: Geophysical Monograph Series.

von Goldbeck, O.K., 1982. Iron−nickel Fe−Ni. In: IRON−Binary Phase Diagrams. Springer Berlin Heidelberg, Berlin, Heidelberg, pp. 73–78.

Hin, R.C., Fitoussi, C., Schmidt, M.W., Bourdon, B., 2014. Experimental determination of the Si isotope fractionation factor between liquid metal and liquid silicate. Earth Planet. Sci. Lett. 387, 55–66. https://doi.org/10.1016/j.epsl.2013.11.016.

Hirose, K., Labrosse, S., Hernlund, J., 2013. Composition and state of the core. Annu. Rev. Earth Planet. Sci. 41 (1), 657–691. https://doi.org/10.1146/annurev-earth-050212-124007.

Hou, M., Liu, J., Zhang, Y., Du, X., Dong, H., Yan, L., Wang, J., Wang, L., Chen, B., 2021. Melting of iron explored by electrical resistance jump up to 135 GPa. Geophys. Res. Lett. 48 (20), 1–10. https://doi.org/10.1029/2021GL095739.

Jackson, J.M., Thomas, C., 2021. Seismic and mineral physics constraints on the D" Layer, pp. 193–227. https://doi.org/10.1002/9781119528609.

Jackson, J.M., Sturhahn, W., Lerche, M., Zhao, J., Toellner, T.S., Alp, E.E., Sinogeikin, S.V., Bass, J.D., Murphy, C.A., Wicks, J.K., 2013. Melting of compressed iron by monitoring atomic dynamics. Earth Planet. Sci. Lett. 362, 143–150. https://doi.org/10.1016/j.epsl.2012.11.048.

Javoy, M., Kaminski, E., Guyot, F., Andrault, D., Sanloup, C., Moreira, M., Labrosse, S., et al., 2010. The chemical composition of the Earth: enstatite chondrite models. Earth Planet. Sci. Lett. 293 (3–4), 259–268. https://doi.org/10.1016/j.epsl.2010.02.033.

Knibbe, J.S., Rivoldini, A., Luginbuhl, S.M., Namur, O., Charlier, B., Mezouar, M., Sifre, D., et al., 2021. Mercury's interior structure constrained by density and P-wave velocity measurements of liquid Fe-Si-C alloys. J. Geophys. Res., Planets 126 (1), 1–26. https://doi.org/10.1029/2020JE006651.

Knibbe, J.S., van Westrenen, W., 2018. The thermal evolution of Mercury's Fe–Si core. Earth Planet. Sci. Lett. 482, 147–159. https://doi.org/10.1016/j.epsl.2017.11.006.

Komabayashi, 2014. Thermodynamics of melting relations in the system Fe-FeO at high pressure: implications for oxygen in the Earth's core. J. Geophys. Res., Solid Earth 119 (5), 4164–4177. https://doi.org/10.1002/2014JB010980.

Komabayashi, T., Fei, Y., Meng, Y., Prakapenka, V., 2009. In-situ X-ray diffraction measurements of the γ-ε transition boundary of iron in an internally-heated diamond anvil cell. Earth Planet. Sci. Lett. 282 (1–4), 252–257. https://doi.org/10.1016/j.epsl.2009.03.025.

Komabayashi, T., Hirose, K., Ohishi, Y., 2012. In situ X-ray diffraction measurements of the Fcc–Hcp phase transition boundary of an Fe–Ni alloy in an internally heated diamond anvil cell. Phys. Chem. Miner. 39 (4), 329–338. https://doi.org/10.1007/s00269-012-0490-3.

Komabayashi, T., Pesce, G., Morard, G., Antonangeli, D., Sinmyo, R., Mezouar, M., 2019a. Phase transition boundary between Fcc and Hcp structures in Fe-Si alloy

and its implications for terrestrial planetary cores. Am. Mineral. 104 (1), 94–99. https://doi.org/10.2138/am-2019-6636.

Komabayashi, T., Pesce, G., Sinmyo, R., Kawazoe, T., Breton, H., Shimoyama, Y., Glazyrin, K., Konôpková, Z., Mezouar, M., 2019b. Phase relations in the system Fe-Ni-Si to 200 GPa and 3900 K and implications for Earth's core. Earth Planet. Sci. Lett. 512, 83–88. https://doi.org/10.1016/j.epsl.2019.01.056.

Labrosse, S., Poirier, J.P., Le Mouël, J.L., 2001. The age of the inner core. Earth Planet. Sci. Lett. 190 (3–4), 111–123. https://doi.org/10.1016/S0012-821X(01)00387-9.

Lay, T., Hernlund, J., Buffett, B.A., 2008. Core-mantle boundary heat flow. Nat. Geosci. 1 (1), 25–32. https://doi.org/10.1038/ngeo.2007.44.

Li, M., 2020. The formation of hot thermal anomalies in cold subduction-influenced regions of Earth's lowermost mantle. J. Geophys. Res. Solid Earth 125 (6), 1–23. https://doi.org/10.1029/2019JB019312.

Lin, J.F., Sturhahn, W., Zhao, J., Shen, G., Mao, H.K., Hemley, R.J., 2004. Absolute temperature measurement in a laser-heated diamond anvil cell. Geophys. Res. Lett. 31 (14), L14611. https://doi.org/10.1029/2004GL020599.

Lord, O.T., Walter, M.J., Dobson, D.P., Armstrong, L., Clark, S.M., Kleppe, A., 2010. The FeSi phase diagram to 150 GPa. J. Geophys. Res. 115 (B6), B06208. https://doi.org/10.1029/2009JB006528.

McDonough, W.F., Sun, S.-s., 1995. The composition of the Earth. Chem. Geol. 120 (3–4), 223–253. https://doi.org/10.1016/0009-2541(94)00140-4.

Morard, G., Andrault, D., Guignot, N., Siebert, J., Garbarino, G., Antonangeli, D., 2011. Melting of Fe–Ni–Si and Fe–Ni–S alloys at megabar pressures: implications for the core–mantle boundary temperature. Phys. Chem. Miner. 38 (10), 767–776. https://doi.org/10.1007/s00269-011-0449-9.

Morard, G., Boccato, S., Rosa, A.D., Anzellini, S., Miozzi, F., Henry, L., Garbarino, G., Mezouar, M., Harmand, M., Guyot, F., Boulard, E., Kantor, I., Irifune, T., Torchio, R., 2018. Solving controversies on the iron phase diagram under high pressure. Geophys. Res. Lett. 45 (20), 11074–11082. https://doi.org/10.1029/2018GL079950.

Morrison, R.A., Jackson, J.M., Sturhahn, W., Zhang, D., Greenberg, E., 2018. Equations of state and anisotropy of Fe-Ni-Si alloys. J. Geophys. Res., Solid Earth 123 (6), 4647–4675. https://doi.org/10.1029/2017JB015343.

Morrison, R.A., Jackson, J.M., Sturhahn, W., Zhao, J., Toellner, T.S., 2019. High pressure thermoelasticity and sound velocities of Fe-Ni-Si alloys. Phys. Earth Planet. Inter. 294, 106268. https://doi.org/10.1016/j.pepi.2019.05.011.

Nomura, R., Hirose, K., Uesugi, K., Ohishi, Y., Tsuchiyama, A., Miyake, A., Ueno, Y., 2014. Low core-mantle boundary temperature inferred from the solidus of pyrolite. Science 343 (6170), 522–525. https://doi.org/10.1126/science.1248186.

Olson, P., 2013. The new core paradox. Science 342 (6157), 431–432. https://doi.org/10.1126/science.1243477.

Ozawa, H., Hirose, K., Mitome, M., Bando, Y., Sata, N., Ohishi, Y., 2009. Experimental study of reaction between perovskite and molten iron to 146 GPa and implications for chemically distinct buoyant layer at the top of the core. Phys. Chem. Miner. 36 (6), 355–363. https://doi.org/10.1007/s00269-008-0283-x.

Prakapenka, V.B., Kubo, A., Kuznetsov, A., Laskin, A., Shkurikhin, O., Dera, P., Rivers, M.L., Sutton, S.R., 2008. Advanced flat top laser heating system for high pressure research at GSECARS: application to the melting behavior of germanium. High Press. Res. 28 (3), 225–235. https://doi.org/10.1080/08957950802050718.

Prakapenka, V., Shen, G., Dubrovinsky, L., 2003. Carbon transport in diamond anvil cells. High Temp., High Press. 35/36 (2), 237–249. https://doi.org/10.1068/htjr098.

Prescher, C., Prakapenka, V.B., 2015. DIOPTAS: a program for reduction of two-dimensional X-ray diffraction data and data exploration. High Press. Res. 35 (3), 223–230. https://doi.org/10.1080/08957959.2015.1059835.

Ricolleau, A., Fei, Y., Corgne, A., Siebert, J., Badro, J., 2011. Oxygen and silicon contents of Earth's core from high pressure metal-silicate partitioning experiments. Earth Planet. Sci. Lett. 310 (3–4), 409–421. https://doi.org/10.1016/j.epsl.2011.08.004.

Sakai, T., Ohtani, E., Hirao, N., Ohishi, Y., 2011. Stability field of the Hcp-structure for Fe, Fe-Ni, and Fe-Ni-Si alloys up to 3 Mbar. Geophys. Res. Lett. 38 (9), 2–6. https://doi.org/10.1029/2011GL047178.

Shahar, A., Ziegler, K., Young, E.D., Ricolleau, A., Schauble, E.A., Fei, Y., 2009. Experimentally determined Si isotope fractionation between silicate and Fe metal and implications for Earth's core formation. Earth Planet. Sci. Lett. 288 (1–2), 228–234. https://doi.org/10.1016/j.epsl.2009.09.025.

Shen, G., Lazor, P., Saxena, S.K., 1993. Melting of Wüstite and iron up to pressures of 600 Kbar. Phys. Chem. Miner. 20 (2), 91–96. https://doi.org/10.1007/BF00207201.

Simon, F., Glatzel, G., 1929. Bemerkungen zur Schmelzdruckkurve. Z. Anorg. Allg. Chem. 178 (1), 309–316. https://doi.org/10.1002/zaac.19291780123.

Sinmyo, R., Hirose, K., Ohishi, Y., 2019. Melting curve of iron to 290 GPa determined in a resistance-heated diamond-anvil cell. Earth Planet. Sci. Lett. 510, 45–52. https://doi.org/10.1016/j.epsl.2019.01.006.

Sohl, F., Schubert, G., 2007. Interior structure, composition, and mineralogy of the terrestrial planets. In: Treatise on Geophysics, vol. 243. Elsevier, pp. 27–68.

Steenstra, E.S., van Westrenen, W., 2020. Geochemical constraints on core-mantle differentiation in Mercury and the aubrite parent body. Icarus 340, 113621. https://doi.org/10.1016/j.icarus.2020.113621.

Sturhahn, W., 2000. CONUSS and PHOENIX: evaluation of nuclear resonant scattering data. Hyperfine Interact. 125 (1–4), 149–172. https://doi.org/10.1023/A:1012681503686.

Sturhahn, W., 2004. Nuclear resonant spectroscopy. J. Phys. Condens. Matter 16 (5), S497–S530. https://doi.org/10.1088/0953-8984/16/5/009.

Sturhahn, W., 2021. MINUTI open source software, version 2.2.0. http://www.nrixs.com.

Sturhahn, W., Jackson, J.M., 2007. Geophysical applications of nuclear resonant spectroscopy. In: Advances in High-Pressure Mineralogy, vol. 421. Geological Society of America, pp. 157–174.

Tateno, S., Komabayashi, T., Hirose, K., Hirao, N., Ohishi, Y., 2019. Static compression of B2 KCl to 230 GPa and its P-V-T equation of state. Am. Mineral. 104 (5), 718–723. https://doi.org/10.2138/am-2019-6779.

Toby, B.H., Von Dreele, R.B., 2013. GSAS-II: the genesis of a modern open-source all purpose crystallography software package. J. Appl. Crystallogr. 46 (2), 544–549. https://doi.org/10.1107/S0021889813003531.

Toellner, T.S., 2000. Monochromatization of synchrotron radiation for nuclear resonant scattering experiments. Hyperfine Interact. 125 (1–4), 3–28. https://doi.org/10.1023/A:1012621317798.

Torchio, R., Boccato, S., Miozzi, F., Rosa, A.D., Ishimatsu, N., Kantor, I., Sévelin-Radiguet, N., et al., 2020. Melting curve and phase relations of Fe-Ni alloys: implications for the Earth's core composition. Geophys. Res. Lett. 47 (14), 1–7. https://doi.org/10.1029/2020GL088169.

Wicks, J.K., Jackson, J.M., Sturhahn, W., Zhang, D., 2017. Sound velocity and density of magnesiowüstites: implications for ultralow-velocity zone topography. Geophys. Res. Lett. 44 (5), 2148–2158. https://doi.org/10.1002/2016GL071225.

Wicks, J.K., Smith, R.F., Fratanduono, D.E., Coppari, F., Kraus, R.G., Newman, M.G., Rygg, J.R., Eggert, J.H., Duffy, T.S., 2018. Crystal structure and equation of state of Fe-Si alloys at super-Earth core conditions. Sci. Adv. 4 (4), eaao5864. https://doi.org/10.1126/sciadv.aao5864.

Zhang, D., Jackson, J.M., Zhao, J., Sturhahn, W., Alp, E.E., Hu, M.Y., Toellner, T.S., Murphy, C.A., Prakapenka, V.B., 2016. Temperature of Earth's core constrained from melting of Fe and Fe0.9Ni0.1 at high pressures. Earth Planet. Sci. Lett. 447, 72–83. https://doi.org/10.1016/j.epsl.2016.04.026.

Zhang, D., Jackson, J.M., Zhao, J., Sturhahn, W., Alp, E.E., Toellner, T.S., Hu, M.Y., 2015. Fast temperature spectrometer for samples under extreme conditions. Rev. Sci. Instrum. 86 (1), 013105. https://doi.org/10.1063/1.4905431.

Zhang, Y., Sekine, T., Lin, J.F., He, H., Liu, F., Zhang, M., Sato, T., Zhu, W., Yu, Y., 2018. Shock compression and melting of an Fe-Ni-Si alloy: implications for the temperature profile of the Earth's core and the heat flux across the core-mantle boundary. J. Geophys. Res., Solid Earth 123 (2), 1314–1327. https://doi.org/10.1002/2017JB014723.